Magnetism of a single atom

Otte, A.F.

Chapter 4

The Kondo Effect of a Single High-Spin Atom

The work presented in this chapter and the following chapter was performed in collaboration with C. F. Hirjibehedin, M. Ternes, C. P. Lutz, and A. J. Heinrich.

4.1 Historical Overview

The story of the Kondo effect starts in the 1930's, when De Haas and coworkers in Leiden measured the resistance of some metals at very low temperatures. They found that surprisingly, the resistance of their gold samples increased rather than decreased when being cooled down below approximately 8 K [54]. Although they already suspected the appearance of this resistance-minimum to be related to the purity of the sample material, the presently accepted explanation was not proposed until 1968 when Kondo attributed the phenomenon to the presence of magnetic impurities [55]. In the following we will discuss the Kondo effect within the framework of the Anderson Impurity Model [56].

4.1.1 Anderson $S = \frac{1}{2}$ Impurity Model

We consider an atomic impurity that is coupled to a bath of electrons with Fermi energy ε_F. The impurity has an orbital that can host two electrons with opposite spin orientations σ ($\uparrow$ or $\downarrow$). Each electron on the impurity has an energy ε_d and if the orbital is doubly filled there is an additional Coulomb repulsion energy U. This can be summarized in the Anderson Hamiltonian:

$$\hat{\mathcal{H}} = \sum_{\sigma} \left\{ \varepsilon_d \hat{d}_\sigma^\dagger \hat{d}_\sigma + \sum_{\mathbf{k}} \varepsilon(\mathbf{k}) \hat{c}_{\mathbf{k}\sigma}^\dagger \hat{c}_{\mathbf{k}\sigma} + \sum_{\mathbf{k}} \left(V \hat{d}_\sigma^\dagger \hat{c}_{\mathbf{k}\sigma} + V^* \hat{c}_{\mathbf{k}\sigma}^\dagger \hat{d}_\sigma \right) \right\} + U \hat{d}_\uparrow^\dagger \hat{d}_\uparrow \hat{d}_\downarrow^\dagger \hat{d}_\downarrow, \tag{4.1}$$

where $\hat{c}_{\mathbf{k}\sigma}^\dagger$ and $\hat{c}_{\mathbf{k}\sigma}$ are the creation and annihilation operators of the electrons in the bath (with wave vector $\mathbf{k}$) while $\hat{d}_\sigma^\dagger$ and $\hat{d}_\sigma$ create and annihilate electrons

on the impurity. The coupling strength between the impurity and the bath is quantified by V. We choose ε_F and ε_d such that the impurity orbital is half filled in its ground state $|d^1_\sigma\rangle$, which thereby becomes degenerate in σ:

$$|d^1_\sigma\rangle = \hat{d}^\dagger_\sigma \prod_{\mathbf{k}}^{\mathbf{k}_F} \hat{c}^\dagger_{\mathbf{k}\uparrow} \hat{c}^\dagger_{\mathbf{k}\downarrow} |\text{vac}\rangle. \tag{4.2}$$

Here $\mathbf{k}_F$ is the Fermi wave vector and $|\text{vac}\rangle$ the vacuum state. For simplicity we also assume that excitations to $|d^2\rangle = \hat{d}^\dagger_{\bar{\sigma}} \hat{c}_{\mathbf{k}\bar{\sigma}} |d^1_\sigma\rangle$ and to $|d^0\rangle = \hat{c}^\dagger_{\mathbf{k}\sigma} \hat{d}_\sigma |d^1_\sigma\rangle$ (where $\bar{\sigma}$ denotes the opposite spin orientation of σ), i.e. respectively adding an electron to or removing an electron from the impurity, cost the same amount of energy $U/2$. As a result the situation becomes electron-hole symmetric: there are two Hubbard bands at the same energy which are each other's mirror image through electron-hole inversion. Effectively the impurity is now a localized $S = \frac{1}{2}$ system that can switch its magnetization through either of two virtual processes, each with a transition rate $2V^2/U$:

$$\begin{array}{ll} |d^1_{\bar{\sigma}}\rangle = \hat{c}^\dagger_{\mathbf{k}'\sigma} \hat{d}_\sigma \hat{d}^\dagger_{\bar{\sigma}} \hat{c}_{\mathbf{k}\bar{\sigma}} |d^1_\sigma\rangle & \text{(i.e. via } |d^2\rangle\text{), or} \\ |d^1_{\bar{\sigma}}\rangle = \hat{d}^\dagger_{\bar{\sigma}} \hat{c}_{\mathbf{k}'\bar{\sigma}} \hat{c}^\dagger_{\mathbf{k}\sigma} \hat{d}_\sigma |d^1_\sigma\rangle & \text{(i.e. via } |d^0\rangle\text{).} \end{array} \tag{4.3}$$

Note that such a process – which has to be energy conserving – can only occur around the Fermi energy as it extracts an electron from the bath and replaces it with an electron that has opposite spin. Therefore it requires both filled and empty states at one energy. By performing a canonical transformation [57], it is possible to approximate (4.1) as:

$$\hat{\mathcal{H}} \simeq \sum_\sigma \sum_{\mathbf{k}} \varepsilon(\mathbf{k}) \hat{c}^\dagger_{\mathbf{k}\sigma} \hat{c}_{\mathbf{k}\sigma} + \frac{2V^2}{U} \sum_{\mathbf{k}\mathbf{k}'} \hat{\mathbf{S}}_d \cdot \hat{\mathbf{S}}_{\mathbf{k}\mathbf{k}'}, \tag{4.4}$$

which is known as the Kondo Hamiltonian. Here $\hat{\mathbf{S}}_d$ is the spin of the impurity and $\hat{\mathbf{S}}_{\mathbf{k}\mathbf{k}'}$ is a second SU(2) (i.e. spin $\frac{1}{2}$) system defined as:

$$\begin{aligned} \hat{S}^+_{\mathbf{k}\mathbf{k}'} &= \hat{c}^\dagger_{\mathbf{k}\uparrow} \hat{c}_{\mathbf{k}'\downarrow}, \\ \hat{S}^-_{\mathbf{k}\mathbf{k}'} &= \hat{c}^\dagger_{\mathbf{k}\downarrow} \hat{c}_{\mathbf{k}'\uparrow}, \\ \hat{S}^z_{\mathbf{k}\mathbf{k}'} &= \frac{1}{2} \left(\hat{c}^\dagger_{\mathbf{k}\uparrow} \hat{c}_{\mathbf{k}'\uparrow} - \hat{c}^\dagger_{\mathbf{k}\downarrow} \hat{c}_{\mathbf{k}'\downarrow} \right). \end{aligned} \tag{4.5}$$

This effective spin can be seen as the net collective magnetization of the electrons in the bath surrounding the impurity, the two spin orientations of which we shall denote as $\Uparrow$ and $\Downarrow$. Since $2V^2/U > 0$, $\hat{\mathbf{S}}_{\mathbf{k}\mathbf{k}'}$ is coupled antiferromagnetically to the impurity spin $\hat{\mathbf{S}}_d$, which is oriented $\downarrow$ and $\uparrow$ respectively. At higher temperatures the system can occupy either of the two degenerate states $|\Downarrow, \uparrow\rangle$ and $|\Uparrow, \downarrow\rangle$. However, if the temperature T sinks below a characteristic Kondo temperature T_K – where $k_B T_K$ is a measure for the coupling strength between bath and impurity – energy can be gained by forming a spin-singlet

Kondo state $\frac{1}{\sqrt{2}}\Big(|\Downarrow,\uparrow\rangle - |\Uparrow,\downarrow\rangle\Big)$ [58]. This leads to a sharp resonance in the electron density of states (DOS) of the Kondo system, exactly at the Fermi energy. Although in quantum mechanics the singlet-triplet formation is a common phenomenon when two doublets are coupled, it should be noted that the current system involves many spins that are distributed over a wide area that has unclear boundaries. The Kondo state is therefore a macroscopic many-body quantum state, the exact properties of which are still under debate in many theoretical studies.

As the conduction electrons in the vicinity of the impurity freeze into this singlet state the transport properties of the conductor change significantly, giving rise to the anomalous increase of the resistance that so much puzzled the Dutch scientists in 1936. But it is important to stress that the Kondo effect itself is not a transport property. In the model discussed above we used only one conducting lead that was coupled to a magnetic impurity. Translated to an STM geometry this means that if a magnetic atom is coupled to the metal surface, the tip is not needed to form a Kondo system. So unlike the inelastic electron excitations of the previous chapters, the Kondo effect just happens; even if you don't measure it.

4.1.2 Experimental Realizations of a Single Kondo Spin

In 1998 research on the Kondo effect experienced a revival when it became possible to experimentally isolate and study a single Kondo-screened spin. This milestone was achieved almost simultaneously through the use of two independently evolved techniques. First, artificially crafted quantum dots in GaAs/AlGaAs semiconductor heterostructures were depleted until they effectively held one electron [59, 60]. The half-integer spin that was thus isolated interacted with neighboring leads via a coupling that could be tuned with great precision. This method provides an extreme level of control that has led to many advanced Kondo experiments [61, 62, 63]. The second technique that enabled the study of individual Kondo spins was the STM, that was used to address individual magnetic atoms lying directly on top of and strongly interacting with a metal surface [64, 65]. Using either method, dI/dV measurements performed on the Kondo system yielded a strong resonance around zero bias voltage. As a hallmark of the Kondo effect, for $T > T_K$ the amplitude of the resonance decreases linearly with the logarithm of T. Its width in energy is a measure for the coupling strength of the Kondo spin to the bath and therefore also for T_K. Typically for magnetic atoms on a metal surface T_K ranges between 50 and 100 K [66], whereas in the quantum dots it can be tuned to values from about 1 K to < 50 mK [60].

Following these first demonstrations, other experimental systems have been found suitable for isolating and addressing an individual Kondo spin as well. These include carbon nanotubes [67, 68, 69] and single-molecule transistors constructed in electromigration junctions [70, 71].

4.2 The Kondo Effect of Co on Cu_2N

In the discussion above we have used an $S = \frac{1}{2}$ impurity. Without losing any of its applicability the model can be generalized to any system with a twofold degenerate ground state, as long as a single-electron process can cause it to switch, i.e. $|\Delta m| = 1$. However, the ground state of a system having $S > \frac{1}{2}$ is more-than-twofold degenerate, making the problem much more complicated. Therefore theoretical considerations of the Kondo effect are often limited to $S = \frac{1}{2}$. Although this assumption is justified for most quantum dot experiments, where the amount of spin on the dot is set precisely to $\frac{1}{2}$, this is not the case in general. Based on their d-shell populations, many magnetic elements have free-atom spin values that are higher and there is no reason to believe that these should all reduce to $\frac{1}{2}$ when the atom is placed upon a surface. Yet the $S = \frac{1}{2}$ model suffices for accurately explaining the Kondo results of such systems. In this section we will investigate this contradiction using the Kondo effect of an $S = \frac{3}{2}$ Co atom on Cu_2N.

4.2.1 Temperature Dependence

As we could already see in fig. 2.2, the spin excitation spectrum of Co on Cu_2N looks dramatically different from the ones obtained on Mn and Fe. The bold curve in fig. 4.1a, taken at 0.5 K, shows apart from a 'regular' spin excitation step at ±5.5 mV a large resonance peak at zero bias. The portion of the spectrum

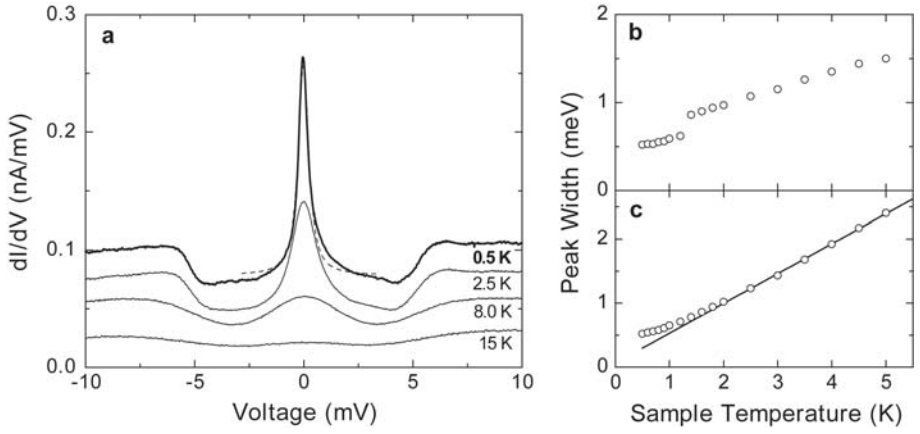

Figure 4.1: (a) Conductance spectra taken on a single Co atom on Cu_2N at various temperatures. Curves measured at temperatures higher than 0.5 K (thin lines) are offset by 0.025 nA/mV each. **(b)** Plot of the full widths at half maximum (FWHM) of the Lorentzian fits (obtained by deconvolution using the sample temperature) versus the sample temperature. **(c)** Similar as (b), but with the approximate tip temperature (0.5 and 1.8 K) used for deconvolution. At higher sample temperatures the plot approaches linear behavior (solid line).

between -3 and 3 mV can be fitted quite well with a thermally broadened Lorentzian (dashed curve), where we use $T = 0.5$ K for the broadening. The Lorentzian lineshape is one of the appearances of the Fano lineshape [72], which is characteristic for the observation of the Kondo effect in an STM configuration [64]. Measurements at higher temperatures are plotted as thinner lines.

Obtaining the Intrinsic Resonance by Deconvolution

In order to identify the peak as a Kondo resonance we should look for an intrinsic temperature dependence in its shape, i.e. a dependence that persist even if the effects of thermal broadening are removed. One quantity that is often plotted as function of temperature is the height of the (deconvoluted) peak, which should decrease linearly with the logarithm of the temperature with a low-temperature roll-off [70, 71]. For STM experiments this is not very useful as the tip height can vary from one measurement to the other because of the normalization condition imposed by the feedback loop. This complication makes the vertical scale of the spectrum uncertain. As an alternative one can also consider the intrinsic width of the spectroscopic feature, which in the case of a Kondo resonance should grow linearly with temperature and at very low temperature saturate at a value $\sim k_B T_K$ [60, 73].

Removing the effects of thermal broadening can be achieved by an iterative deconvolution procedure that involves repeatedly fitting the curve with a convoluted lineshape [73]:

$$\frac{dI}{dV}(V,T) \propto \int_{-\infty}^{\infty} \rho_{\mathrm{s}}(\varepsilon,T)\frac{d}{dV}f(\varepsilon - eV,T)d\varepsilon. \tag{4.6}$$

Here $\rho_{\mathrm{s}}(\varepsilon,T)$ is the intrinsic DOS of the sample we would like to extract (note that in case of a Kondo effect it can still depend on T), while we assume the tip DOS to be independent of either ε or T. The above expression also includes the Fermi-Dirac distribution function

$$f(\varepsilon,T) = \frac{1}{\mathrm{e}^{\varepsilon/k_B T}+1}, \tag{4.7}$$

the voltage-derivative of which is a Gaussian peak with full width at half maximum (FWHM) $3.2k_BT$. Apart from the temperature, also the voltage modulation we add to the bias for lock-in detection broadens the spectroscopic features. In the following, whenever we refer to deconvolution performed with a temperature T, we actually use an effective temperature giving rise to a Gaussian with an effective FWHM of $\sqrt{\left(3.2k_BT/e\right)^2 + \left(2\sqrt{2}V_{\mathrm{mod}}\right)^2}$ [74], where V_{mod} is the RMS modulation voltage (in this case 50 μV).

In fig. 4.1b the full widths at half maximum of the deconvoluted Lorentzian fits are plotted against the temperature of the sample T_{s} (as read off from the thermometer mounted on the scanner), where for each curve T_{s} (combined with the modulation broadening) was used for the deconvolution. The plot shows a sharp discontinuity between 1.2 and 1.4 K, which corresponds to the switching

point between two different cooling methods: measurements at $T_s \leq 1.2$ K were performed in single-shot mode whereas at $T_s > 1.2$ K the ^{3}He was flowing continuously (section 1.4). This jump is likely to be caused by unequal tip and sample temperatures. Both the thermometer and the heater were thermally anchored strongly to the sample, whereas the tip was cooled almost directly by the liquid ^{3}He without being influenced much by heating. Therefore in many cases the temperature of the tip was much lower than the thermometer indicated. In the following paragraph we will discuss the influence of unequal tip and sample temperatures on the thermal broadening in tunneling spectroscopy and the proper treatment of this discrepancy in the deconvolution process.

Thermal Broadening with Unequal Temperatures

In general the net tunnel-current I flowing from tip to sample can be expressed as the difference between the currents caused by electrons tunneling from tip to sample $I_{t\to s}$ and vice versa $I_{s\to t}$ [74]:

$$\begin{aligned} I &= I_{t\to s} - I_{s\to t} \\ &\propto \frac{4\pi e}{\hbar}\int_{-\infty}^{\infty}\Big\{\rho_t(\varepsilon - eV)\rho_s(\varepsilon)f(\varepsilon - eV, T_t)\Big(1 - f(\varepsilon, T_s)\Big) \\ &\qquad -\rho_t(\varepsilon - eV)\rho_s(\varepsilon)f(\varepsilon, T_s)\Big(1 - f(\varepsilon - eV, T_t)\Big)\Big\}d\varepsilon \\ &\propto \frac{4\pi e}{\hbar}\int_{-\infty}^{\infty}\rho_t(\varepsilon - eV)\rho_s(\varepsilon)\Big(f(\varepsilon - eV, T_t) - f(\varepsilon, T_s)\Big)d\varepsilon. \end{aligned} \tag{4.8}$$

Here $\hbar$ is the reduced Planck constant while $\rho_t(\varepsilon)$ and $\rho_s(\varepsilon)$ are the densities of states of the tip and sample respectively. Again $f(\varepsilon, T)$ is the Fermi-Dirac distribution function that in this case can depend on either tip temperature T_t or sample temperature T_s. In the above expression we assume that the tunneling matrix element coupling the tip and the sample is independent of energy (hence the proportionality sign). Taking the derivative to V we find:

$$\begin{aligned} \frac{dI}{dV} \propto \frac{4\pi e}{\hbar}\int_{-\infty}^{\infty}\Big\{&\frac{d}{dV}\Big[\rho_t(\varepsilon - eV)\Big]\rho_s(\varepsilon)f(\varepsilon - eV, T_t) \\ &+\rho_t(\varepsilon - eV)\rho_s(\varepsilon)\frac{d}{dV}\Big[f(\varepsilon - eV, T_t)\Big] \\ &-\frac{d}{dV}\Big[\rho_t(\varepsilon - eV)\Big]\rho_s(\varepsilon)f(\varepsilon, T_s)\Big\}d\varepsilon. \end{aligned} \tag{4.9}$$

If we assume the tip DOS to be independent of energy and we once more allow the intrinsic DOS of the sample to depend on T_s, the expression reduces to:

$$\frac{dI}{dV} \propto \frac{4\pi e}{\hbar}\int_{-\infty}^{\infty}\rho_t\rho_s(\varepsilon, T_s)\frac{d}{dV}f(\varepsilon - eV, T_t)d\varepsilon. \tag{4.10}$$

Comparing this to (4.6), we see that remarkably, in absence of thermal equilibrium the thermal broadening is caused exclusively by the temperature of the tip, provided that its DOS is flat.

As no sensor was connected to the tip, we can only estimate its temperature. We will therefore assume that the tip was not sensitive to heating and adopted only two different temperatures; one corresponding to each cooling method. For the measurements taken in single-shot mode ($T_\mathrm{s} \leq 1.2$ K) we use $T_\mathrm{t} = 0.5$ K. As shown in fig. 4.1c, choosing $T_\mathrm{t} = 1.8$ K for the continuous flow measurements ($T_\mathrm{s} > 1.2$ K) causes the two segments of data points to line up very well[1]. Now we see that the temperature dependence of the intrinsic width approaches linear behavior (with a slope of $5.4 \pm 0.1 k_B$) at high temperatures, whereas at low temperature it saturates as expected for a Kondo resonance. If we follow the convention of choosing the zero-temperature FWHM of the resonance to be $2k_B T_K$ we find a Kondo temperature $T_K = 2.7 \pm 0.2$ K. For the extrapolation to zero temperature we assume the width – being determined by whichever is the highest of T_K and T_s – to go like $\sqrt{\left(2k_B T_K\right)^2 + \left(5.4 k_B T_\mathrm{s}\right)^2}$.

4.2.2 Why Co is Kondo-Screened

Now that we have established the presence of a Kondo resonance in Co on Cu_2N, the question arises why it appears in this specific case and why no such effect is observed in either Mn or Fe on Cu_2N. Let us therefore once more review the requirements for a Kondo effect. As discussed in section 4.1.1, in order for a spin to become Kondo-screened it needs to have a twofold degenerate ground state which is coupled to a bath of electrons. Also, the difference in the magnetization quantum number, $|\Delta m|$, should be equal to 1 in order to enable electrons to initiate the virtual switching process. In chapter 3 we found that both Mn and Fe have a negative axial anisotropy parameter D, causing the high $|m|$ values to be favored over the lower values. For Mn this leads to a twofold degenerate ground state with $|\Delta m| = 5$ while for Fe $|\Delta m| = 4$. Moreover, as in the latter case the transverse anisotropy parameter E is finite, the ground state of Fe is not even degenerate. So we find that for these two atoms Kondo behavior can be easily excluded based on their magnetic anisotropy. Similarly, the anisotropy of Co on Cu_2N can – as we will see in this section – explain why this particular atom does become Kondo-screened.

[1] For continuous flow mode, 1.8 K is somewhat high (1.4 K would have been expected). However, forcing the tip temperature to 1.4 K in continuous flow would suggest it to become significantly smaller than 0.5 K in single shot which is highly unrealistic. Nonetheless, this freedom in fixing tip temperatures has been taken into account in determining the error in T_K. The larger than expected difference between the two T_t values does not influence our statement that this is a Kondo resonance. By choosing it to be 1.8 K for the $T_\mathrm{s} = 1.4$ K peak we assign more of its width to thermal broadening, yet the remaining width is still much larger than that of the intrinsic $T_\mathrm{s} = 0.5$ K resonance.

Kramers Degeneracy

Kramers' degeneracy theorem states that in an arbitrarily asymmetric but purely electrostatic (crystal) field, any system that consists of an odd number of electrons (and therefore has a half-integer spin) will remain at least twofold degenerate in the absence of a magnetic field [75]. This follows from the time reversal invariance of a Hamiltonian that describes an electrostatic field, of which our anisotropy Hamiltonian (3.3) is an example if we choose $\mathbf{B} = 0$. The consequence of this statement is that for Mn ($S = \frac{5}{2}$) and Co (which has $3d^7$, so probably $S = \frac{3}{2}$; we will verify this later) the zero-field degeneracy between states with equal $|m|$ cannot be broken by a finite E value unlike the case of Fe ($S = 2$).

It is illustrative to verify this theorem by perturbation theory. Since by definition $E \leq \frac{1}{3}D$ (otherwise the axes are reassigned), we will treat the transversal anisotropy term as a perturbation, i.e.:

$$\hat{\mathcal{H}} = \overbrace{-g\mu_B \mathbf{B}\cdot\hat{\mathbf{S}} + D\hat{S}_{\mathcal{Z}}^2}^{\hat{\mathcal{H}}_0} + \overbrace{E\left(\hat{S}_{\mathcal{X}}^2 - \hat{S}_{\mathcal{Y}}^2\right)}^{\hat{\mathcal{H}}'}. \tag{4.11}$$

The eigenstates of $\hat{\mathcal{H}}_0$ are simply the $|m\rangle$ states, whereas in general $\hat{\mathcal{H}}'$ mixes these. Using $\hat{S}_\pm = \hat{S}_{\mathcal{X}} \pm i\hat{S}_{\mathcal{Y}}$ we can rewrite the Hamiltonian to:

$$\hat{\mathcal{H}} = \hat{\mathcal{H}}_0 + \frac{E}{2}\left(\hat{S}_+^2 + \hat{S}_-^2\right). \tag{4.12}$$

Now it becomes evident that $\hat{\mathcal{H}}'$ to first order only couples states that have $\Delta m = \pm 2$ and to higher order only if $\Delta m = \pm 2n$, where n is an integer (this is why in the case of Fe the $|m| = 2$ states are split much less than the $|m| = 1$ states: it is only a higher order correction). So the perturbation mixes the $|m\rangle$ states, but does so only from two separate subgroups. For example, if $S = 2$ the resulting eigensystem will consist of three states that are linear combinations of $|+2\rangle$, $|+0\rangle$ and $|-2\rangle$ and two states that are linear combinations of $|+1\rangle$ and $|-1\rangle$. Here, original eigenstates with equal $|m|$ are coupled by the perturbation giving rise to avoided crossings, i.e. lifted degeneracies. But if $S = \frac{3}{2}$, the combinations are $|+\frac{3}{2}\rangle$ and $|-\frac{1}{2}\rangle$ on the one hand and $|+\frac{1}{2}\rangle$ and $|-\frac{3}{2}\rangle$ on the other, leaving the degeneracy in $|m|$ untouched. This is true for any half-integer spin and although here we have discussed it only in approximation, the result is exact and holds for any value of E.

The Role of Anisotropy

As we did before for Mn and Fe, we can use the spin excitation energies to determine the anisotropy parameters. In the zero-field spectrum of fig. 4.1a there is one pair of steps symmetrically at ±5.5 mV (measurements up to ±25 mV did not reveal additional excitations). Assuming that Co maintains its free-atom spin value of $S = \frac{3}{2}$ and taking Kramers degeneracy into account, these steps can either be assigned to $|\pm\frac{1}{2}\rangle \rightarrow |\pm\frac{3}{2}\rangle$ excitations if $D < 0$, or to

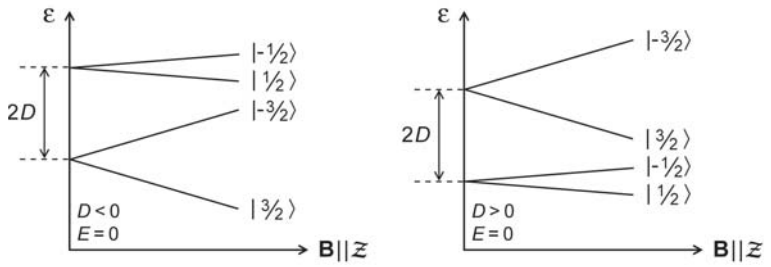

Figure 4.2: (a) Qualitative energy diagrams for an uniaxially anisotropic $S = \frac{3}{2}$ system with negative and positive values of D, with the field oriented along the unique axis. For $D > 0$, a low-energy $|\pm\frac{1}{2}\rangle$ Kramers doublet is formed.

$|\pm\frac{3}{2}\rangle \rightarrow |\pm\frac{1}{2}\rangle$ if $D > 0$ (for now we will neglect E as it cannot influence the zero-field excitations anyhow). Figure 4.2 shows qualitative energy diagrams for either situation. If D were negative, the situation would be very similar to Mn with a twofold degenerate ground state having $|\Delta m| = 3$. However, for $D > 0$ the two ground states are separated by $|\Delta m| = 1$: the ideal system for Kondo-screening!

In the next section we will show by field-dependent measurements that this interpretation (i.e. $S = \frac{3}{2}$, $D > 0$) is indeed correct. Not only does that make this the first report of a Kondo effect in a known high-spin (i.e. $S > \frac{1}{2}$) system, it also demonstrates the importance of magnetic anisotropy in enabling the Kondo effect. By breaking the degeneracy in $|m|$, the crystal field reduces the large spin into an effective $S = \frac{1}{2}$ Kramers doublet that can become Kondo-screened at low temperatures. This finding, which agrees with theoretical predictions on

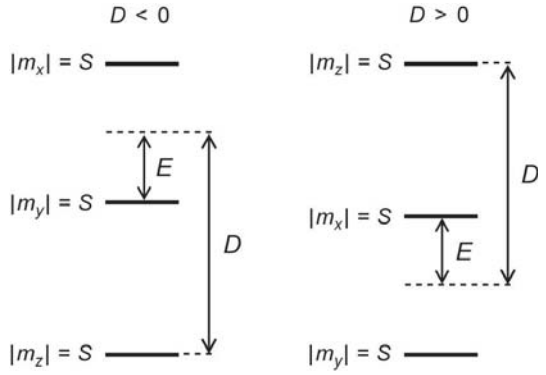

Figure 4.3: (a) Energy eigenvalues of (3.3) with $\mathbf{B} = 0$ and E just smaller than $|D|/3$ for negative and positive values of D, in case maximum magnetization is assigned to each of the primary axes. Physically the two situations are almost identical, yet one is labelled 'easy-axis' and the other 'hard-axis'. This picture is valid for any $S > \frac{1}{2}$.

the role of anisotropy in a Kondo system [76, 77], implies that Co in a different environment might not show any Kondo effect at all. Similarly, atoms with half-integer spin that are not a Kondo system in one case (like Mn on Cu_2N) may become so in another situation. In fact, this could retrospectively explain previous findings in [18] where Mn atoms on Al_2O_3 islands on a NiAl surface were studied by spin excitation spectroscopy. Although no Kondo behavior was observed on most of them, some atoms (presumably Mn, as judged from their apparent height) that were located close to the edge of an island did show a zero-bias resonance that was attributed to Kondo-screening. This might very well be caused by a local change in the anisotropy energies.

The interpretation presented above also raises some questions. Because although each anisotropic system can be discretely labelled as either 'easy-axis'($D < 0$) or 'hard-axis'/'easy-plane' ($D > 0$), the boundary separating these two possibilities is quite subtle. In fig. 4.3 two situations are depicted schematically, each having an E-value that is only slightly smaller than $\frac{1}{3}|D|$ but with different signs of D. Physically the two situations are very close, except for rearrangement of the axes, yet according to our model one of them should result in a Kondo resonance and the other not at all. It is unclear how the system would precisely behave in this crossover region.

4.3 A Kondo Spin and Its Environment

When a sufficiently large magnetic field B is applied to a Kondo-screened spin, Zeeman splitting will lift the degeneracy in its ground state (4.2) as a result of which the Kondo effect is quenched. However, for smaller fields where the Zeeman energy is comparable to $k_B T_K$, what remains of the Kondo-resonance peak splits into two peaks. This was observed both in quantum dot [59, 60] and STM Kondo systems [18]. The effect of a magnetic field can be incorporated into the Anderson Hamiltonian (4.1) by making ε_f spin-dependent: $\varepsilon_{f\uparrow} = \varepsilon_{f0} - \Delta\varepsilon/2$ and $\varepsilon_{f\downarrow} = \varepsilon_{f0} + \Delta\varepsilon/2$, where $\Delta\varepsilon$ is the Zeeman energy. Calculations based on this model predict the splitting between the peaks in the DOS to be $2\Delta\varepsilon$ [78, 79]. Although these calculations are beyond the scope of this thesis, we can verify their result through a simple model.

Let us start in state $|d^1_\downarrow\rangle$ which is $\Delta\varepsilon = g\mu_B B$ higher in energy than the ground state $|d^1_\uparrow\rangle$. We will now flip its spin by performing one of the virtual processes of (4.3):

$$|d^1_\uparrow\rangle = \hat{c}^\dagger_{\mathbf{k}'\downarrow}\hat{d}_\downarrow\hat{d}^\dagger_\uparrow\hat{c}_{\mathbf{k}\uparrow}|d^1_\downarrow\rangle. \tag{4.13}$$

The energy that was lost by the impurity spin during this process has been absorbed by the bath in the form of an electron-hole excitation. In order to get back to the original situation we can for example perform the following operation:

$$|d^1_\downarrow\rangle = \hat{d}^\dagger_\downarrow\hat{c}_{\mathbf{k}'\downarrow}\hat{c}^\dagger_{\mathbf{k}\uparrow}\hat{d}_\uparrow|d^1_\uparrow\rangle, \tag{4.14}$$

where the impurity reclaims the lost energy from the bath by destroying the electron-hole pair. Note that during the entire exercise the whole system was

excited by $g\mu_B B$. If we would have started in the true ground state of the system $|d^1_\uparrow\rangle$ (and the Fermi sea unexcited), none of the above could happen because the impurity has no source to extract energy from. The Kondo resonance therefore takes place at an energy $\varepsilon_F + g\mu_B B$, but since the situation is electron-hole symmetric (because we chose the energy to ionize the impurity to be $U/2$ either way) it shows up as two peaks at $V = \pm g\mu_B B/e$ in the conductance spectrum.

Incidentally, those are exactly the positions where we expect to find the dI/dV steps in spin excitation spectroscopy. Of course that is not surprising: after all it is the same spin excitation that now occurs resonantly *at* the excitation energy rather than driven by tunneling electrons *at and beyond* the excitation energy. Therefore it appears as a peak rather than a step in the differential conductance. Consequently we can expect the split peaks to follow the positions of the spin-excitation steps whenever the excitation energies are changed. In the remainder of this chapter we will verify this hypothesis by modifying the excitations through various environmental factors. First we will study the evolution of the peak positions under the influence of a magnetic field in combination with the strong magnetic anisotropy that the Cu_2N surface provides. In section 4.3.2 other atomic spins will be placed near the Kondo-screened Co atom, giving rise to changes in the excitation spectra due to spin-coupling.

4.3.1 Anisotropic Field Dependence

Figures 4.4b-d show spin excitation spectra taken on individual Co atoms, each corresponding to a different field direction. As expected the peak splits into two, but the rate at which it splits depends strongly on the field direction. Plotting the observed excitation energies against the field strength (fig. 4.5) suggests that whereas the $\mathbf{B} \parallel x$ and $\mathbf{B} \parallel z$ directions yield very similar spectra, both the step and peak positions are markedly different for $\mathbf{B} \parallel y$. Such anisotropic field dependence of the Kondo peak positions has not been observed before and is a noteworthy result that is directly related to the high-spin nature of the system. A true $S = \frac{1}{2}$ system cannot be sensitive to magnetic anisotropy as presented in (3.3) because none of the second-order $|\Delta m| = 1$ terms can link the $|\pm\frac{1}{2}\rangle$ eigenstates. So even though the crystal field has reduced the Co spin to an *effective* spin $\frac{1}{2}$ as far as creating a Kondo system is concerned, it clearly still carries the signature of a true high-value spin.

Since we want to use these spectra for studying the relation of the peak positions to the underlying excitation energies, we will mainly use the step positions for determining the anisotropy parameters of Co on Cu_2N. Especially when taking into account the $\sim 5\%$ variations in the excitation energies that were encountered between different atoms of the same kind in chapter 3, we can consider the $\mathbf{B} \parallel x$ and $\mathbf{B} \parallel z$ dependence to be sufficiently equal to model this system exclusively with uniaxial anisotropy (i.e. $E = 0$ and $\mathcal{Z} = y$). However, it is important to realize once more that even if E would have been finite, Kramers' theorem would have prevented it from harming the degeneracy needed for Kondo-screening. Fitting the step positions to the energy of the

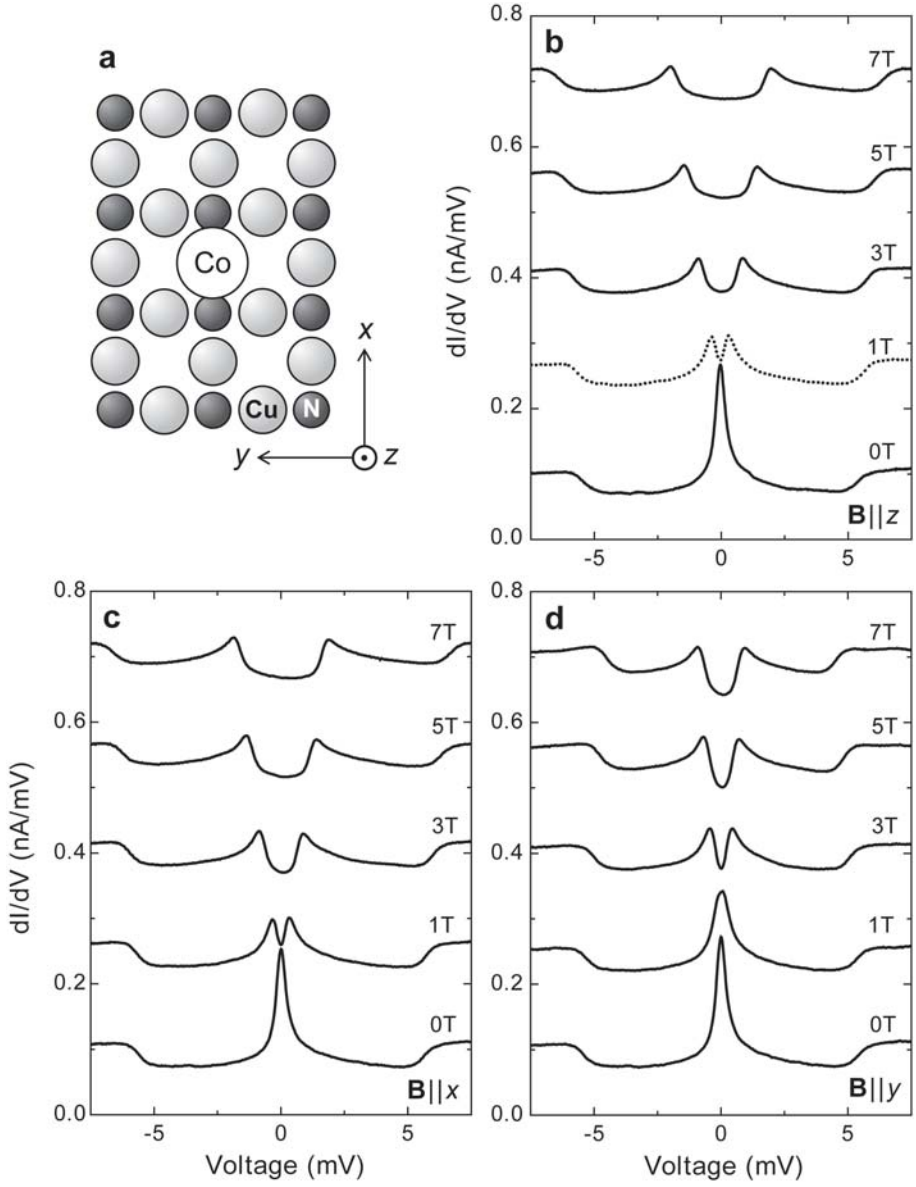

Figure 4.4: (a) Axis-assignment for Co on Cu_2N (identical to what was used earlier for Mn and Fe). **(b–d)** dI/dV-spectra on individual Co atoms in various magnetic fields oriented along z, x and y in (b), (c) and (d) respectively. Curves corresponding to non-zero fields are offset by 0.15 nA/mV. The dotted spectrum in (b) was measured on a different atom than those with other field strengths in the same direction.

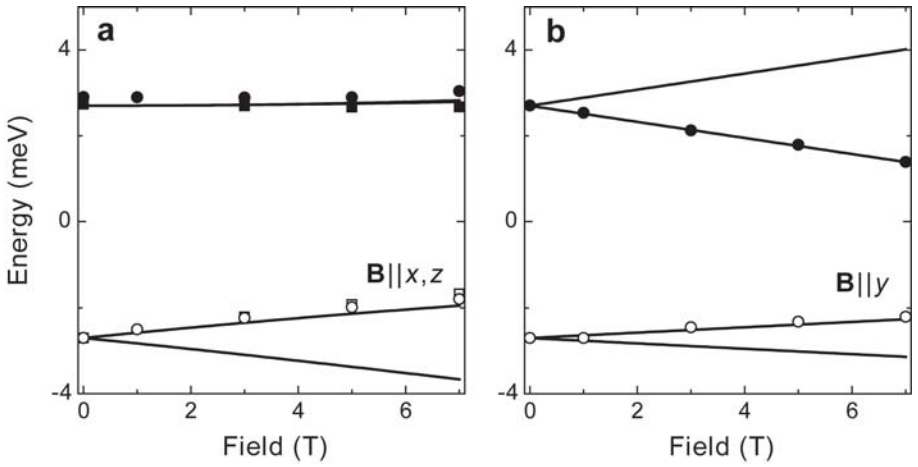

Figure 4.5: Graphs of the peak and step positions taken from fig. 4.4b–d against the field strength for $\mathbf{B}||x$ (circles) and $\mathbf{B}||z$ (squares) in **(a)** and $\mathbf{B}||y$ in **(b)**. Peak (*step*) positions are indicated by open (*filled*) symbols. For the x and z-directions the peak positions are quite similar and therefore hard to distinguish. In contrast to the graphs presented in chapter 3 showing directly the measured excitation energies, here the final energies at the end of the excitation process are plotted: each data point indicates a measured excitation energy added to the calculated ground state energy at the corresponding field. Accordingly, the solid lines show the calculated eigenenergies (rather than the calculated excitation energies as before).

second excitation yields[2] $g = 2.1 \pm 0.2$ and $D = 2.7 \pm 0.1$ meV, indicating that our reasoning in section 4.2.2 – which was based on hard-axis anisotropy ($D > 0$) – was indeed correct. The solid lines in fig. 4.5 show the calculated eigenenergies of the anisotropy Hamiltonian for these values.

At this point we turn to the field dependence of the peaks in the spectra. According to our understanding of the Kondo effect, the peaks should closely follow the $|+\frac{1}{2}\rangle \rightarrow |-\frac{1}{2}\rangle$ excitation energies. As can be seen from the open symbols in fig. 4.5 they do so very well for all field directions. The data points seem to be consistently slightly high compared to the calculated energy, but this might result from the fact that the maximum of a peak that is superimposed on top of an upward step (which should still be there) is shifted towards higher values. Although not surprising, this result is quite remarkable: the entire model we used to calculate the transition energies was based on the anisotropy of a single spin in a one-particle picture, yet it precisely captures the behavior of the many-body Kondo system.

[2]The error margins here are much larger than for Mn and Fe. This probably results from forcing E to be 0. Leaving E free as a fit-parameter unfortunately does not resolve this problem, since the $|+\frac{1}{2}\rangle \rightarrow |+\frac{3}{2}\rangle$ energy is very insensitive to changes in E which can therefore not be determined. However, the choice of $E = 0$ is justified by the similarity of the $|+\frac{1}{2}\rangle \rightarrow |-\frac{1}{2}\rangle$ excitations (i.e. the peaks) – which *are* sensitive to transverse anisotropy – in the $\mathbf{B} \parallel x$ and $\mathbf{B} \parallel z$ measurements.

4.3.2 Coupled Kondo Systems

Having studied the interplay of a Kondo-screened spin with nonmagnetic atoms (i.e. the crystal field), we now shift our attention to the influence of magnetic atoms on a Kondo impurity. Similar studies in quantum dots [80] and electromigration junctions [81] have shown remarkable changes in the properties of a Kondo system through spin-spin coupling. The ease with which vertical atom manipulation can be performed on Cu_2N makes this an ideal surface for doing such experiments in an STM configuration. Here we will discuss various measurements performed on a class of atomic structures that exhibit spin-coupling that is of the proper strength to compete with the effects of magnetic anisotropy and Zeeman splitting.

Weak Coupling Through Vacancies

As shown schematically in fig. 4.6a, a magnetic atom "X" (which can be Fe, Mn or Co) and a Co atom are separated by 7.2 Å along a vacancy row. Such a structure is built by first positioning either one of the atoms on a Cu site and than placing the second atom on one of the two N sites closest to the desired final position (dashed circle in the figure, assuming the Co atom was positioned first). Finally the atom is hopped in place by a 1.5 V pulse (see section 2.3.3) with $\sim$ 50 % success rate[3]. In the following we will refer to such structures using the shorthand "$X_{vv}Co$" (where the v's correspond to the two vacancy sites between the atoms).

These nano-engineered structures differ in three ways from those used in earlier spin-coupling studies on Cu_2N [19], where **(1)** the inter-atomic spacing was half as large, i.e. 3.6 Å, **(2)** the atoms were positioned along a N-row rather than a v-row and **(3)** all atoms were identical (Mn). In that situation the atoms were coupled quite strongly (because of their proximity as well as the high electron density along the N-rows) as a result of which they formed one entity, both in topography and in spectroscopy. Also, once constituted the structures could not be controllably disassembled. In contrast, in a topograph of the current dimers (fig. 4.6b) one can clearly recognize each constituent atom. Each of these can be removed without causing lasting damage and be replaced by a different atom at will. As we will see shortly, at these relative positions the two atoms produce individual excitation spectra that still resemble those of the corresponding single atoms and the effects of spin-coupling on the Co atom are comparable in magnitude to the field-induced splitting of the previous section.

In fig. 4.6b we see three vertically oriented dimers: a $Mn_{vv}Co$ (atoms 1 and 2), a $Fe_{vv}Co$ (atoms 3 and 4) and a $Co_{vv}Co$ structure (atoms 5 and 6). The horizontally oriented dimer on the central island is $Co_{vv}Co$ as well. Each combination was built in both orientations to enable field-direction dependent measurements (in the current image the magnetic field was oriented vertically). In addition each structure was built once more on a sample where the field was

[3]We did not perform statistics on the success rate of hopping so this number is based on general impression. If any, there might be a slight bias in favor of success.

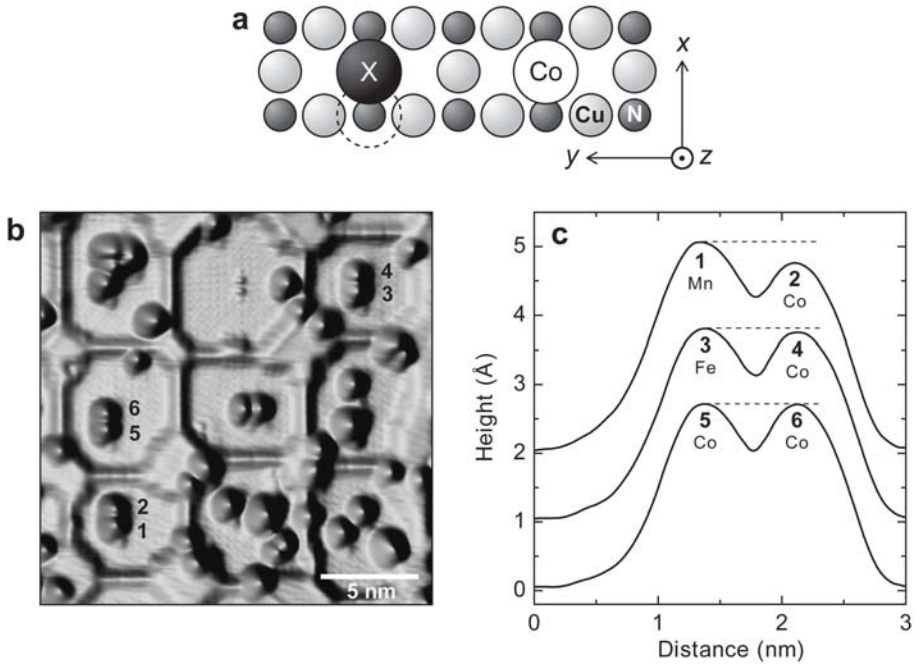

Figure 4.6: **(a)** Structural drawing of the $X_{vv}Co$ dimer with axis-assignments. The dashed circle indicates where the second atom has to be put down in case the Co atom was positioned first. **(b)** Topographic image (20×20 nm, 10 mV/1 nA) showing four dimers on separate Cu_2N islands: one $Mn_{vv}Co$ (atoms 1 and 2), one $Fe_{vv}Co$ (atoms 3 and 4) and two $Co_{vv}Co$'s (atoms 5 and 6 and the structure on the central island). **(c)** Height profiles taken from (b) in vertical direction. The zero of the lower profile corresponds to the surface of the Cu_2N island; the other two are offset by 1 Å each. The dashed lines are meant as a guide to compare the apparent heights of the atoms.

oriented perpendicular to the surface. All dimers where placed such that no lattice defect, island edge or other adatom was present within a range of 14.4 Å (i.e. 4 unit cells). As fig. 4.6c shows, the apparent height (at 10 mV/1 nA) of the Fe and Co atoms was nearly identical whereas that of Mn was slightly higher. Because the combination of two Kondo-screened spins in the $Co_{vv}Co$ structures introduces an extra complication we will first focus on the effects of coupling non-Kondo spins to Co.

The World's Tiniest Compass

The lowest curves in fig. 4.7 show the zero-field spectra for each of the two atoms in $Fe_{vv}Co$ (for this the same atom-lock procedure was used as discussed in section 2.3.1 for measurements on individual atoms). Although the typical Co spectrum can still be recognized by its spin excitation steps, the central Kondo feature has changed dramatically: the resonance peak seems to have split

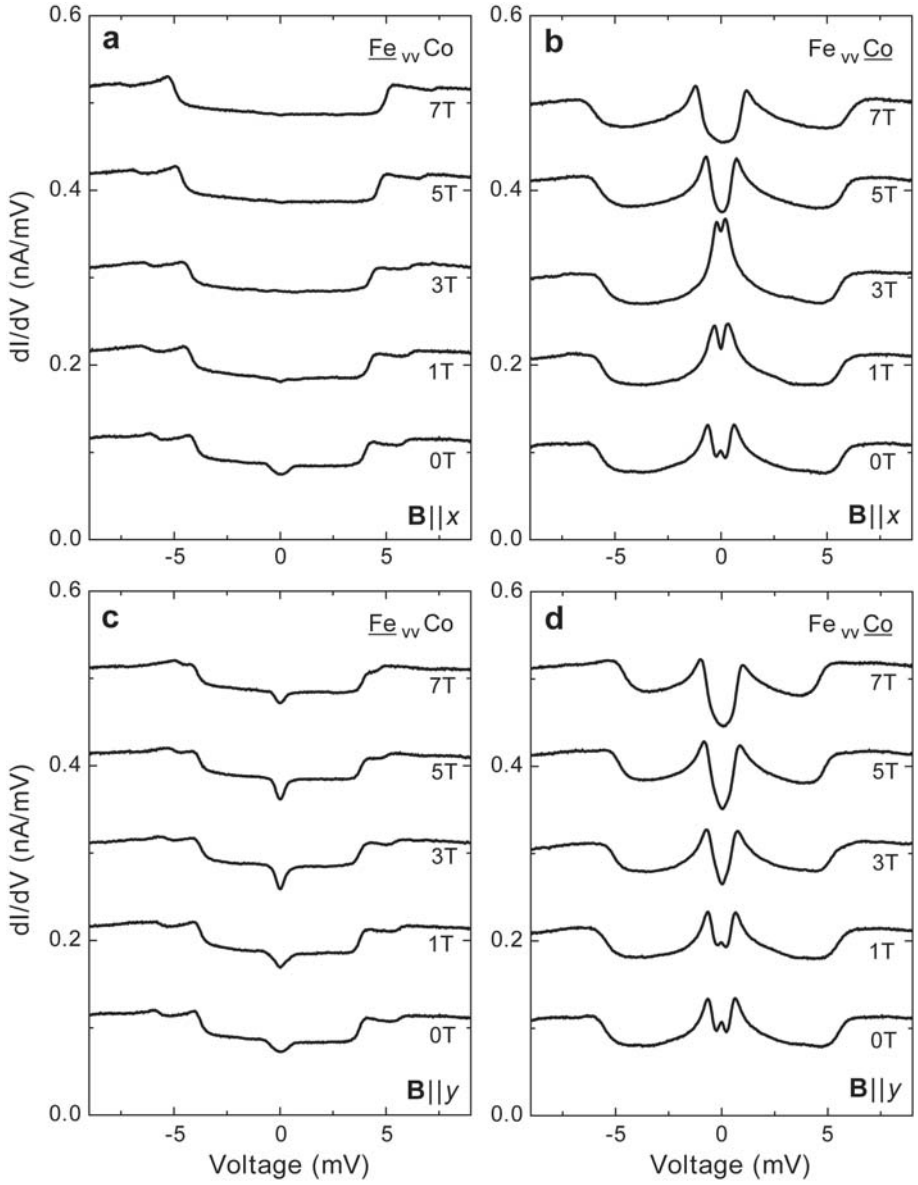

Figure 4.7: dI/dV-spectra measured on $Fe_{vv}Co$ when the tip was positioned over the Fe atom **(a, c)** and Co atom **(b, d)** at various magnetic fields oriented along x (a, b) and y (c, d).

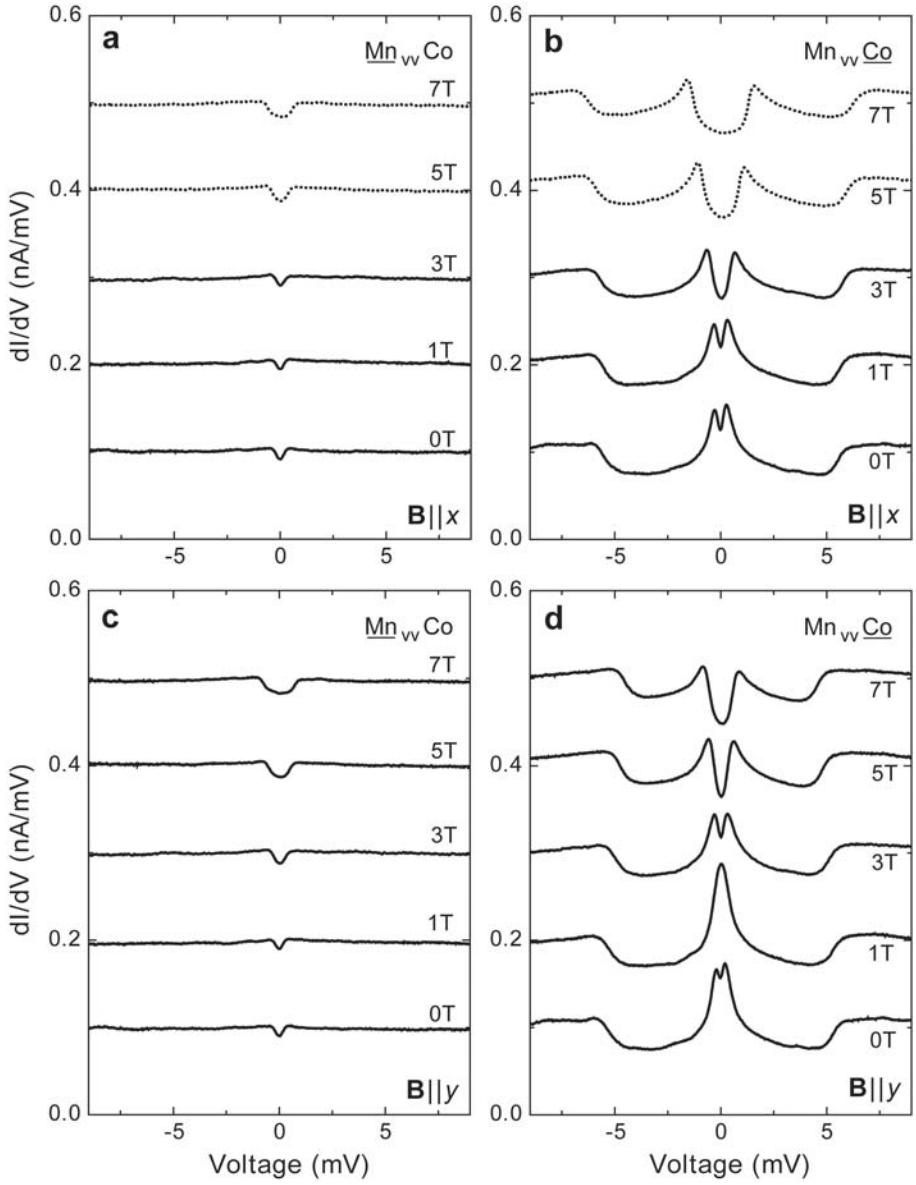

Figure 4.8: dI/dV-spectra measured on $Mn_{vv}Co$ with the tip over the Mn atom **(a, c)** and Co atom **(b, d)** at various magnetic fields oriented along x (a, b) and y (c, d). Dotted spectra were taken on a different structure (identical but built elsewhere on the Cu_2N surface) than those with other field strengths in the same direction.

and a small extra peak has appeared at zero-bias. If we neglect this central peak for now (it will be taken into consideration further on) it looks like the proximity of the Fe atom is experienced by the Co atom as an effective magnetic field.

This interpretation is confirmed surprisingly well by measurements at finite fields. If $\mathbf{B} \parallel x$ (i.e. measured on the horizontal structure in fig. 4.6b) the separation between the two peaks decreases until $B \simeq 2$ T after which it grows again. If however $\mathbf{B} \parallel y$ no such crossing occurs: the separation stays roughly constant and grows only slightly beyond $B \sim 3$ T. Measurements at $\mathbf{B} \parallel z$ (to be discussed further on[4] in chapter 5, fig. 5.11a) indicate qualitatively similar behavior as for $\mathbf{B} \parallel y$. So it seems as if the external magnetic field is able to cancel the effect induced by the Fe atom's effective field if it is oriented along x, but cannot do so in the other directions. The Co atom experiences a net field $B_{\text{net}} = |\mathbf{B}+\mathbf{B}_{\text{eff}}|$, where the effective field $\mathbf{B}_{\text{eff}}$ points in the opposite direction of the external magnetic field's x-component. As a result $B_{\text{net}} = B - B_{\text{eff}}$ if $\mathbf{B} \parallel x$ and $B_{\text{net}} = \sqrt{B^2 + B_{\text{eff}}^2}$ if $\mathbf{B} \perp x$. This result is in excellent agreement with our knowledge of Fe: in chapter 3 we found that the spin of an individual Fe atom on Cu_2N has the x-axis as its easy-axis along which it likes to magnetize even in the absence of an external magnetic field. If an external field is applied the Fe spin will always align with its x-component and therefore by symmetry the field lines of the Fe atom's field must oppose the external field's x-component at the position of the Co atom.

This qualitative 'effective field' picture also fits reasonably well for the results on $Mn_{vv}Co$ (figs. 4.8 and 5.11b). Here the peaks cross around $B \simeq 1$ T if $\mathbf{B} \parallel y$ or $\mathbf{B} \parallel z$ but repel each other if $\mathbf{B} \parallel x$. With the exception of the crossing when $\mathbf{B} \parallel y$, again this agrees with our finding that Mn has an easy-axis along z. It should be noted, however, that the anisotropy energy of Mn is much weaker than that of Fe ($D = -0.039$ meV and -1.55 meV respectively). Therefore the preferred magnetization direction of the Mn spin might be more easily disturbed by a perpendicular field.

Thus a single Co atom acts as the world's tiniest compass: it locally probes the direction and strength of the magnetic field around a single atomic spin. Clearly this picture is highly simplistic and incomplete in many ways: the concept of field lines is not applicable to quantum spins, the atoms can no longer be treated individually and as we will discuss in section 4.4 the dipolar field of such a spin system would be far too weak to be measured at a distance of 7.2 Å. Yet the concept of such an effective magnetic field beautifully captures the essence of these experiments. It demonstrates the stunning amount of control with which individual atoms can be handled and proves that even deep inside the realm of quantum mechanics, as a first approximation our classical intuition may still guide us. And, as we will see shortly, it certainly is not incorrect.

[4]These measurements were performed with a special tip that will not be discussed until section 5.3. However, this is not expected to influence the energies at which the peaks and steps are encountered.

4.3.3 Full Heisenberg Model

In this section we will try to model the spin-coupled systems of the previous section quantitatively by combining the Zeeman effect, magneto-crystalline anisotropy and spin-coupling in one Hamiltonian. In order to do so we need to merge two spin systems that in general have Hilbert spaces with different dimensionalities. For this purpose we will use tensor multiplication as discussed in [82]. If for example we combine an $S = \frac{1}{2}$ system and an $S = 1$ system, being described by spin-state vectors

$$|m_a\rangle = \begin{pmatrix} a_1 \\ a_2 \end{pmatrix} \qquad \text{and} \qquad |m_b\rangle = \begin{pmatrix} b_1 \\ b_2 \\ b_3 \end{pmatrix}, \tag{4.15}$$

all resulting states are represented by the tensor product of $|m_a\rangle$ and $|m_b\rangle$:

$$|m_a\rangle \otimes |m_b\rangle = \left(\begin{array}{c} a_1b_1 \\ a_1b_2 \\ a_1b_3 \\ \hline a_2b_1 \\ a_2b_2 \\ a_2b_3 \end{array}\right) \equiv |m_a\ m_b\rangle. \tag{4.16}$$

Here the horizontal line only acts as a guide to the eye and has no algebraic significance. Similarly one can tensor-multiply operators, e.g. $\hat{A}$ (2×2) working on $|m_a\rangle$ and $\hat{B}$ (3×3) working on $|m_b\rangle$:

$$\hat{A} \otimes \hat{B} = \left(\begin{array}{c|c} A_{11}\hat{B} & A_{12}\hat{B} \\ \hline A_{21}\hat{B} & A_{22}\hat{B} \end{array}\right), \tag{4.17}$$

where the A_{mn}'s refer to the matrix elements of $\hat{A}$. If we want to perform an operation on only one of the spins we should tensor-multiply with the identity $\hat{\mathbb{I}}$ on the other side, e.g.:

$$\begin{aligned} \left(\hat{S}_y|m_a\rangle\right) \otimes |m_b\rangle = \left(\hat{S}_y \otimes \hat{\mathbb{I}}\right)|m_a\ m_b\rangle &= \begin{pmatrix} 0 & -i \\ i & 0 \end{pmatrix} \otimes \begin{pmatrix} 1 & 0 & 0 \\ 0 & 1 & 0 \\ 0 & 0 & 1 \end{pmatrix} |m_a\ m_b\rangle \\ &= \left(\begin{array}{ccc|ccc} & & & -i & & \\ & & & & -i & \\ & & & & & -i \\ \hline i & & & & & \\ & i & & & & \\ & & i & & & \end{array}\right) |m_a\ m_b\rangle \equiv \hat{S}_y^{(a)}|m_a\ m_b\rangle. \end{aligned} \tag{4.18}$$

Similarly, $\hat{S}_y^{(b)}|m_a\ m_b\rangle \equiv \left(\hat{\mathbb{I}} \otimes \hat{S}_y\right)|m_a\ m_b\rangle$, where now $\hat{S}_y$ is the corresponding

spin operator with the dimension of $|m_b\rangle$. Using this formalism we can begin constructing our Hamiltonian. As in [19] we will model the interaction between the two spins with an isotropic Heisenberg coupling term:

$$\hat{\mathcal{H}} = J\hat{\mathbf{S}}^{(a)} \cdot \hat{\mathbf{S}}^{(b)} = J\left(\hat{S}_x^{(a)}\hat{S}_x^{(b)} + \hat{S}_y^{(a)}\hat{S}_y^{(b)} + \hat{S}_z^{(a)}\hat{S}_z^{(b)}\right), \tag{4.19}$$

where J is the coupling constant. The spins tend to align ferromagnetically for $J < 0$ whereas $J > 0$ leads to antiferromagnetic relative orientation.

Let us start with the case of $Fe_{vv}Co$. Combining (4.19) with the Zeeman and anisotropy terms (3.3) for each of the two spins we can form the following Hamiltonian[5]:

$$\begin{aligned}\hat{\mathcal{H}} &= J\hat{\mathbf{S}}^{(\mathrm{Fe})} \cdot \hat{\mathbf{S}}^{(\mathrm{Co})} - \mu_B \mathbf{B} \cdot \left(g_{\mathrm{Fe}}\hat{\mathbf{S}}^{(\mathrm{Fe})} + g_{\mathrm{Co}}\hat{\mathbf{S}}^{(\mathrm{Co})}\right) \\ &\quad + D_{\mathrm{Fe}}\hat{S}_x^{2(\mathrm{Fe})} + E_{\mathrm{Fe}}\left(\hat{S}_y^{2(\mathrm{Fe})} - \hat{S}_z^{2(\mathrm{Fe})}\right) + D_{\mathrm{Co}}\hat{S}_y^{2(\mathrm{Co})}.\end{aligned} \tag{4.20}$$

Note that here we have adopted the axis assignments that we found for the single atoms: $(\mathcal{X}, \mathcal{Y}, \mathcal{Z}) = (y, z, x)$ for Fe and $\mathcal{Z} = y$ for Co. Again, we choose to model Co with uniaxial anisotropy (i.e. $E_{\mathrm{Co}} = 0$). During the following analysis we will allow the other anisotropy parameters D_{Co}, D_{Fe} and E_{Fe}, as well as g_{Co} and g_{Fe} to deviate no more than 5% from their single atom values. This way the Heisenberg coupling parameter J remains as the only fully free fitting parameter of (4.20). Since the $Fe_{vv}Co$ system has 20 eigenstates it is very difficult to fit all excitation energies simultaneously via an automated routine. The presented 'fits' were found by manually adjusting the parameter values and can therefore not be guaranteed to be optimal. However, we will see that the results are very convincing and cannot be far off.

The Low-Energy Case: One Spin Fixed

In fig. 4.9 the first four calculated energy levels, obtained by diagonalization of (4.20), are plotted for $J = 0.13$ meV and $\mathbf{B} \parallel x$ together with the peak positions extracted from fig. 4.7b (still neglecting the central peak). Except for an avoided crossing around 1.1 T, caused by the finite value of E_{Fe}, the diagram consists of two pairs of diverging levels that are shifted vertically relative to each other by $\sim J$. According to these pairs we label the states $|\psi_{\alpha 0}\rangle, |\psi_{\alpha 1}\rangle, |\psi_{\beta 0}\rangle$ and $|\psi_{\beta 1}\rangle$. Obviously this labelling is not defined at the avoided crossing, but we will only use it for field values well away from it. Due to the difference in slopes we see that at 2.1 T the ground state switches from $|\psi_{\alpha 0}\rangle$ to $|\psi_{\beta 0}\rangle$.

These four levels can almost entirely be expressed within the subspace spanned by the eight $|m_{\mathrm{Fe}}| = 2$ states, i.e. $|m_{\mathrm{Fe}}\ m_{\mathrm{Co}}\rangle = |\pm 2 \pm \frac{1}{2}\rangle$ and $|\pm 2 \pm \frac{3}{2}\rangle$ where the m's refer to the eigenvalues of $\hat{S}_x^{(\mathrm{Fe})}$ and $\hat{S}_x^{(\mathrm{Co})}$. Table 4.1 lists the corresponding coefficients both for $B = 0$ T and for 4 T along x. Here some small

[5] For terms like $\hat{S}_x^{2(\mathrm{Fe})}$ it does not matter whether the square is taken before or after the tensor product, i.e. $\left(\hat{S}_x \otimes \hat{\mathbb{I}}\right)^2 = \hat{S}_x^2 \otimes \hat{\mathbb{I}}$.

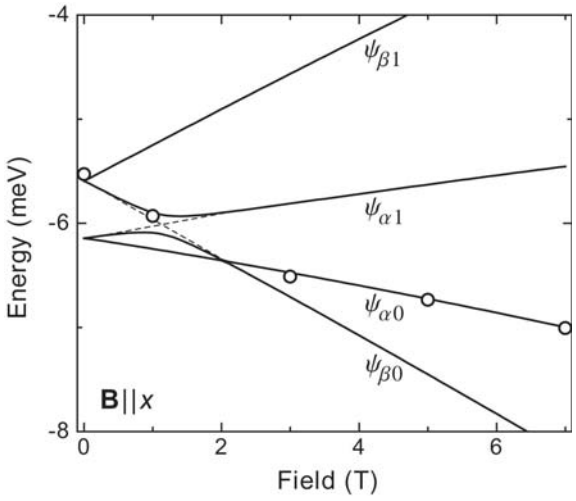

Figure 4.9: Lowest four eigenvalues of (4.20) with $J = 0.13$ meV, $g_{\mathrm{Fe}} = 2.11$, $g_{\mathrm{Co}} = 2.16$, $D_{\mathrm{Fe}} = -1.53$ meV, $E_{\mathrm{Fe}} = 0.31$ meV and $D_{\mathrm{Co}} = 2.70$ meV for $B = 0$ to 7 T along x. Two crossing dashed lines indicate what the energy levels would be like if $E_{\mathrm{Fe}} = 0$. The levels are labelled according to this situation: $\{\psi_{\alpha 0}, \psi_{\alpha 1}, \psi_{\beta 0}, \psi_{\beta 1}\}$ with ascending energy at $B = 0$. Open circles indicate the positions where peaks were encountered in the corresponding spectra of fig. 4.7b, all plotted with respect to the calculated ground state (i.e. as in fig. 4.5). Here the small zero-bias peak in the 0 T spectrum was omitted.

contributions of $m_{\mathrm{Fe}} = 0$ resulting from finite E_{Fe} are neglected, the largest matrix element of which is 0.16. From the coefficients we can see that at either value of B the strongly diverging levels $|\psi_{\beta 0}\rangle$ and $|\psi_{\beta 1}\rangle$ have most weight in states where the two spins have parallel orientation (remember that the expectation value is the square of the matrix element), whereas $|\psi_{\alpha 0}\rangle$ and $|\psi_{\alpha 1}\rangle$ are mostly oriented antiparallel. Note that the higher values of $|m_{\mathrm{Co}}|$ are preferred over the lower ones because $\mathbf{B}$ points in the x-direction which is part of the easy-plane of Co.

The peak positions that were measured over the Co atom, the data points in fig. 4.9, coincide very well with $|\psi_{\alpha 0}\rangle \rightarrow |\psi_{\beta 0}\rangle$ excitations when $B < 2.1$ T, while above the change of ground state they closely follow $|\psi_{\beta 0}\rangle \rightarrow |\psi_{\alpha 0}\rangle$. This is not surprising since the $|\psi_{\alpha 0}\rangle$ and $|\psi_{\beta 0}\rangle$ states are almost identical through inversion of m_{Co}: by parking the tip over the Co atom we can flip its spin from antiparallel to parallel or vice versa with respect to the Fe atom's spin, while leaving the Fe spin itself untouched. Access to the other two states, $|\psi_{\alpha 1}\rangle$ and $|\psi_{\beta 1}\rangle$, requires exciting the Fe spin and can therefore not be gained while the tip is over the Co atom. At $B = 2.1$ T the ground state is incidentally degenerate as a result of which the Co spin can once more become Kondo-screened, leading to the reconstructed resonance peak we observed. This effect is not found if the tip is positioned over the Fe atom because in that situation the electrons do not tunnel directly into the resonance, which takes place only on the Co atom.

Table 4.1: Projection of eigenvectors for $Fe_{vv}Co$, obtained by diagonalization of (4.20) with $J = 0.13$ meV, $g_{Fe} = 2.11$, $g_{Co} = 2.16$, $D_{Fe} = -1.53$ meV, $E_{Fe} = 0.31$ meV, $D_{Co} = 2.70$ meV and $B = 0$ T and 4 T along x, on the subspace of $|m_{Fe}\ m_{Co}\rangle$ states with $|m_{Fe}| = 2$. Matrix elements outside this subspace are no larger than 0.16. The states are labelled based on their physical significance rather than their eigenvalues (fig. 4.9): $\{\psi_{\alpha 0}, \psi_{\alpha 1}, \psi_{\beta 0}, \psi_{\beta 1}\}$ with ascending energy at $B = 0$ T and $\{\psi_{\beta 0}, \psi_{\alpha 0}, \psi_{\alpha 1}, \psi_{\beta 1}\}$ with ascending energy at $B = 4$ T.

State	$\|+2{+}\frac{3}{2}\rangle$	$\|+2{+}\frac{1}{2}\rangle$	$\|+2{-}\frac{1}{2}\rangle$	$\|+2{-}\frac{3}{2}\rangle$	$\|-2{+}\frac{3}{2}\rangle$	$\|-2{+}\frac{1}{2}\rangle$	$\|-2{-}\frac{1}{2}\rangle$	$\|-2{-}\frac{3}{2}\rangle$
$B = 0$ T								
$\|\psi_{\alpha 0}\rangle$	0	0.46	0	–0.86	0	0	0	0
$\|\psi_{\alpha 1}\rangle$	0	0	0	0	–0.86	0	0.46	0
$\|\psi_{\beta 0}\rangle$	0.82	0	–0.53	0	0	0	0	0
$\|\psi_{\beta 1}\rangle$	0	0	0	0	0	–0.53	0	0.82
$B = 4$ T								
$\|\psi_{\alpha 0}\rangle$	0	–0.53	0	0.84	0	0	0	0
$\|\psi_{\alpha 1}\rangle$	0	0	0	0	–0.90	0	0.40	0
$\|\psi_{\beta 0}\rangle$	0.88	0	–0.46	0	0	0	0	0
$\|\psi_{\beta 1}\rangle$	0	0	0	0	0	–0.61	0	0.78

Tip-Position Dependent Transition Intensities

We will now expand our analysis to include higher-energy excitations as well as excitations of the Fe spin. In order to accurately sort out which of the large set of eigenstates are accessible through inelastic electron excitations we will use the transition intensity calculations that were introduced in section 3.3.3. We simulate the position of the tip by assuming that only the spin closest to the tip can be excited, e.g.[6]:

$$I_{0\to n}^{(\mathrm{Fe})} = \left|\langle\psi_n|\,\hat{S}_x^{(\mathrm{Fe})}\,|\psi_0\rangle\right|^2 + \left|\langle\psi_n|\,\hat{S}_y^{(\mathrm{Fe})}\,|\psi_0\rangle\right|^2 + \left|\langle\psi_n|\,\hat{S}_z^{(\mathrm{Fe})}\,|\psi_0\rangle\right|^2, \qquad (4.21)$$

where $I_{0\to n}^{(\mathrm{Fe})}$ is the transition intensity from the ground state to $|\psi_n\rangle$ when the tip is over the Fe atom. As the multitude of states is much larger than before it is worthwhile to combine the intensity information together with the energy levels in one single graph which will now be introduced step by step.

The small dots in figs. 4.10 and 4.11 show the lowest 12 eigenenergies of (4.20) in magnetic field intervals of 0.1 T along x and y respectively. As before, proper parameter values for these calculations were found by manual tuning. The dots representing the ground state $|\psi_0\rangle$ are colored black while the coloring of the remaining levels $|\psi_n\rangle$ is based on $I_{0\to n}^{(\mathrm{Co})}$ and $I_{0\to n}^{(\mathrm{Fe})}$ (see color key in fig. 4.11). Red

[6]Note that here we drop the suggestive labelling used in the previous section and once more number the states $|\psi_n\rangle$ with increasing energy.

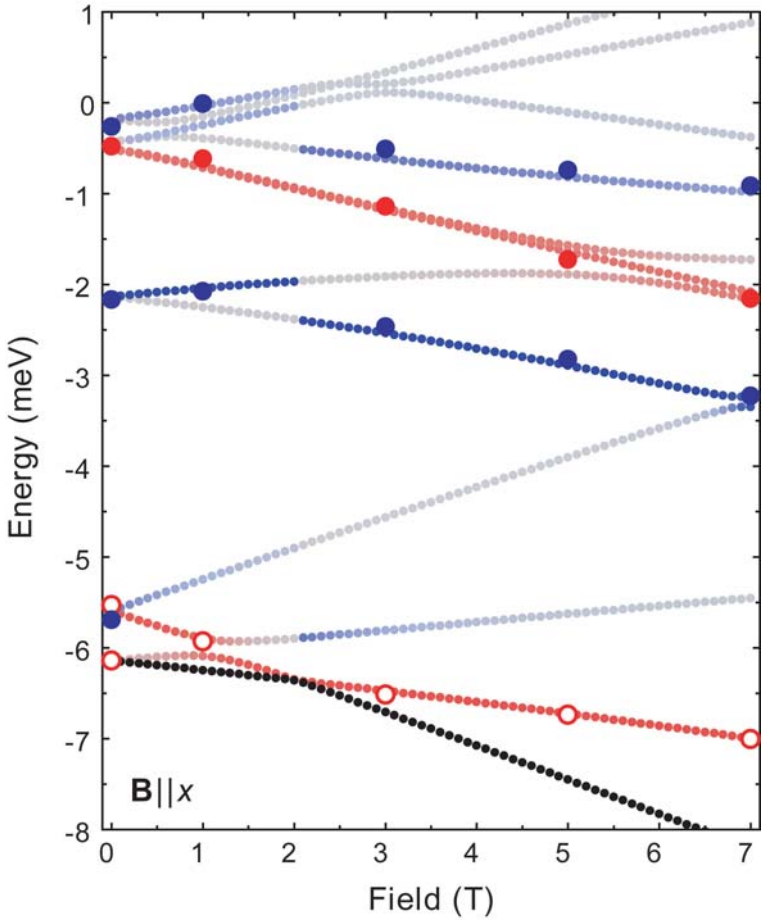

Figure 4.10: Small dots: lowest 12 eigenvalues of (4.20) with $J = 0.13$ meV, $g_{\mathrm{Fe}} = 2.11$, $g_{\mathrm{Co}} = 2.16$, $D_{\mathrm{Fe}} = -1.53$ meV, $E_{\mathrm{Fe}} = 0.31$ meV and $D_{\mathrm{Co}} = 2.70$ meV for $B = 0$ to 7 T in increments of 0.1 T along x. Color indicates the values of $I^{(\mathrm{Co})}_{0\to n}$ (red) and $I^{(\mathrm{Fe})}_{0\to n}$ (blue); see fig. 4.11 for key. The ground state is colored black. Large dots: experimental data points indicating positions of peaks (open circles) and steps (filled circles) in figs. 4.7a (blue, Fe) and b (red, Co), all plotted with respect to the calculated ground state.

dots correspond to a high value of $I^{(\mathrm{Co})}_{0\to n}$ (i.e. a high transition intensity towards that level if the tip is positioned over Co) while blue dots have a high $I^{(\mathrm{Fe})}_{0\to n}$. If neither intensity is high the dot becomes grey: it represents a state that is not expected to be accessible through tunneling excitation through either atom. States that can be reached both via excitations on Co and on Fe are colored magenta. In both graphs the blue excitations between -3 and 0 meV represent excitations towards $|m_{\mathrm{Fe}}| = 1$; the red line between -2 and 0 meV consists of

two excitations that involve rotating the Co spin towards its hard-axis[7]. Note that here we use our knowledge of the intensities only qualitatively: a transition is either possible or not.

Experimental data, taken from fig. 4.7, is added to the graph as larger dots: red for features found in Co spectra and blue for Fe. Open circles correspond to peak positions (local maximum in dI/dV) while closed circles refer to steps (maximum in $|d^2I/dV^2|$). The agreement is evident: data points appear almost exclusively on energy levels that have the appropriate color. In a few instances (such as the low-energy Fe step at $B = 1$ T along y) the dot ends up between two correctly colored lines (in this case magenta). In those situations the energy resolution of the measurement was insufficient to separately distinguish two individual excitations. The highest-energy Fe excitations for $\mathbf{B} \parallel y$ that lie close to lines that are only faintly blue correspond to steps that only have a relatively small height as seen in fig. 4.7c.

The point where the ground state changes, $B = 2.1$ T along x, has a very clear signature in the higher-energy excitations too: both Fe transitions suddenly switch to a different level. Let us focus on the lower of the two (around -2 meV) by expressing the involved levels at the critical field within the subspace of $|m_{\mathrm{Fe}}| = 1$ states (in the $|m_{\mathrm{Fe}}\ m_{\mathrm{Co}}\rangle$-basis, with ground state $|\psi_0\rangle$):

$$|\psi_4\rangle = -0.65|{+1}{+\tfrac{3}{2}}\rangle - 0.30|{+1}{-\tfrac{1}{2}}\rangle + 0.59|{-1}{+\tfrac{3}{2}}\rangle + 0.35|{-1}{-\tfrac{1}{2}}\rangle, \quad \text{and}$$
$$|\psi_5\rangle = -0.70|{+1}{-\tfrac{3}{2}}\rangle + 0.43|{+1}{+\tfrac{1}{2}}\rangle + 0.46|{-1}{-\tfrac{3}{2}}\rangle - 0.30|{-1}{+\tfrac{1}{2}}\rangle,$$

where matrix elements ≤ 0.10 are ignored. Again, these two states almost only differ in the sign of m_{Co}. Comparing their coefficients to the ones listed in table 4.1, we see that through $\Delta|m_{\mathrm{Fe}}| = 1$ transitions $|\psi_4\rangle$ is linked to $|\psi_{\beta 0}\rangle$ (ground state above 2.1 T) while $|\psi_5\rangle$ is linked to $|\psi_{\alpha 0}\rangle$ (ground state below 2.1 T). The external magnetic field flipping the nearby Co spin is felt on the Fe atom which is reflected beautifully in the corresponding spin excitations.

Let us do the same thing for $\mathrm{Mn_{vv}Co}$. For this system the full Heisenberg Hamiltonian becomes:

$$\begin{aligned}\hat{\mathcal{H}} &= J\hat{\mathbf{S}}^{(\mathrm{Mn})} \cdot \hat{\mathbf{S}}^{(\mathrm{Co})} - \mu_B \mathbf{B} \cdot \left(g_{\mathrm{Mn}} \hat{\mathbf{S}}^{(\mathrm{Mn})} + g_{\mathrm{Co}} \hat{\mathbf{S}}^{(\mathrm{Co})} \right) \\ &\quad + D_{\mathrm{Mn}} \hat{S}_z^{2(\mathrm{Mn})} + D_{\mathrm{Co}} \hat{S}_y^{2(\mathrm{Co})},\end{aligned} \tag{4.22}$$

where we neglect E_{Mn} which in the case of a single Mn atom was only 0.007 meV. This system has 24 eigenstates which are all plotted for $J = 0.06$ meV with the two in-plane field directions up to 7 T in figs. 4.12 and 4.13. In either case the states appear in two bundles of 12 that are separated by $2D_{\mathrm{Co}}$. The color coding for the intensities is similar as before except that blue now refers to $I_{0\to n}^{(\mathrm{Mn})}$. On the Co atom excitations can be made towards the high bundle, which as before involves rotating the spin towards its hard-axis, whereas Kondo resonances only

[7] As the vertical scales of these graphs have an arbitrary zero, these specific energy values have no physical significance and are only mentioned for visual reference.

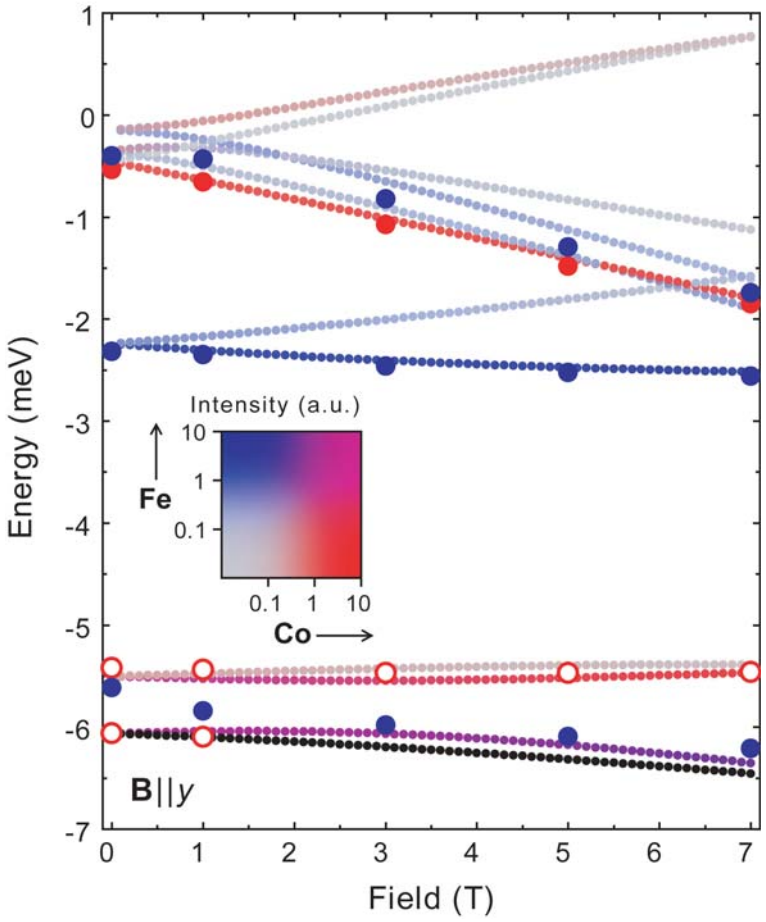

Figure 4.11: Lowest 12 eigenvalues of (4.20) with $J = 0.13$ meV, $g_{\rm Fe} = 2.11$, $g_{\rm Co} = 2.16$, $D_{\rm Fe} = -1.48$ meV, $E_{\rm Fe} = 0.33$ meV and $D_{\rm Co} = 2.70$ meV for $\mathbf{B} \parallel y$, represented as in fig. 4.10. Experimental data points extracted from figs. 4.7c (blue) and d (red). **Inset:** key for the color representation of $I^{(\rm Co)}_{0\to n}$ and $I^{(\rm Fe)}_{0\to n}$.

occur within the lower bundle. The Mn spin can excite towards the $m_{\rm Mn} = \frac{3}{2}$ states in the lower bundle where $m_{\rm Mn}$ refers to the eigenvalue of $\hat{S}^{(\rm Mn)}_z$. Each of these predicted transitions is observed exactly at the correct energy.

Although by far not as clear as with $\rm Fe_{vv}Co$ also here a cancellation effect, giving rise to the reconstructed Kondo peak, can be discerned. When $B \simeq 1$ T along y, the red/magenta line that carries the low-energy Co excitation comes very close to the ground state – much closer then it does for $\mathbf{B} \parallel x$. It is this intersection of ground states that tells us the correct value of the Heisenberg constant: $J = 0.03 \pm 0.02$ meV for $\rm Mn_{vv}Co$ and $J = 0.13 \pm 0.02$ meV for

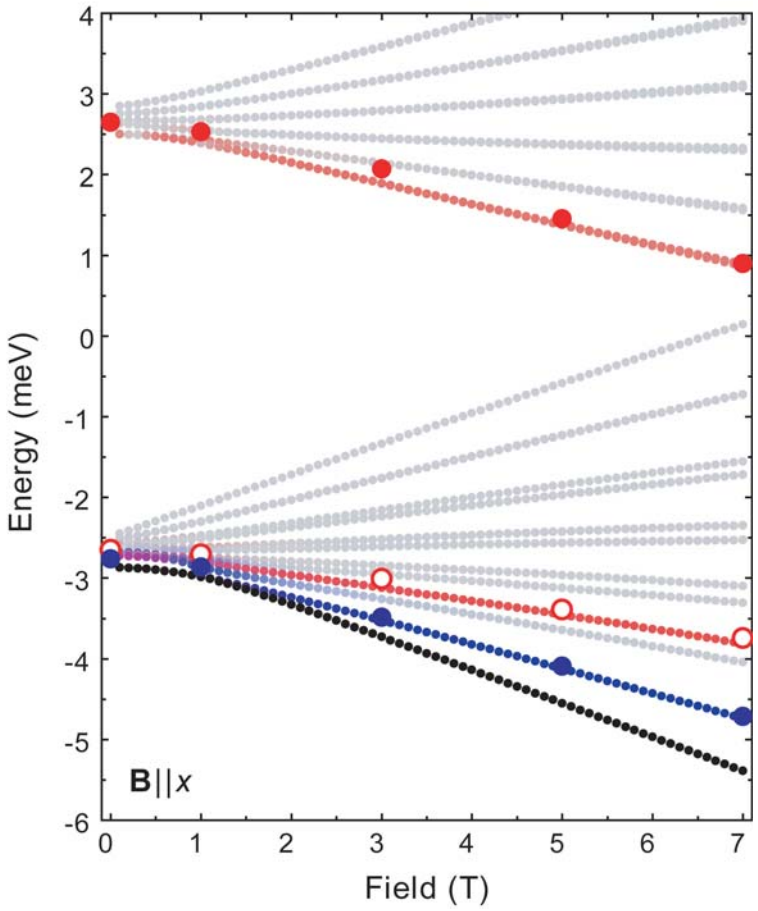

Figure 4.12: Eigenvalues of (4.22) with $J = 0.03$ meV, $g_{\mathrm{Mn}} = 1.90$, $g_{\mathrm{Co}} = 2.16$, $D_{\mathrm{Mn}} = -0.04$ meV and $D_{\mathrm{Co}} = 2.65$ meV for $\mathbf{B} \parallel x$. See fig. 4.13 for key of color representation of $I^{(\mathrm{Co})}_{0\to n}$ and $I^{(\mathrm{Mn})}_{0\to n}$. Experimental data points extracted from figs. 4.8a (blue) and b (red), plotted with respect to the calculated ground state. Open (*filled*) circles represent peak (*step*) positions.

$\mathrm{Fe_{vv}Co}$. But what about the effective field that was introduced in section 4.3.2? Well, it really is the same thing. If we reduce either (4.20) or (4.22) to a single Co spin Hamiltonian by fixing the other spin (i.e. by throwing away all terms that contain no operators working on the Co spin) we find:

$$\hat{\mathcal{H}} = -g_{\mathrm{Co}}\mu_B \left(\mathbf{B} - \frac{J\mathbf{S}^{(\mathrm{X})}}{g_{\mathrm{Co}}\mu_B} \right) \cdot \hat{\mathbf{S}}^{(\mathrm{Co})} + D_{\mathrm{Co}} \hat{S}_y^{2(\mathrm{Co})}, \tag{4.23}$$

where (X) is either (Fe) or (Mn). Here $\mathbf{S}^{(\mathrm{X})}$ no longer needs to be an operator as it does not work on the Co spin anyhow. The proximity of the second spin is

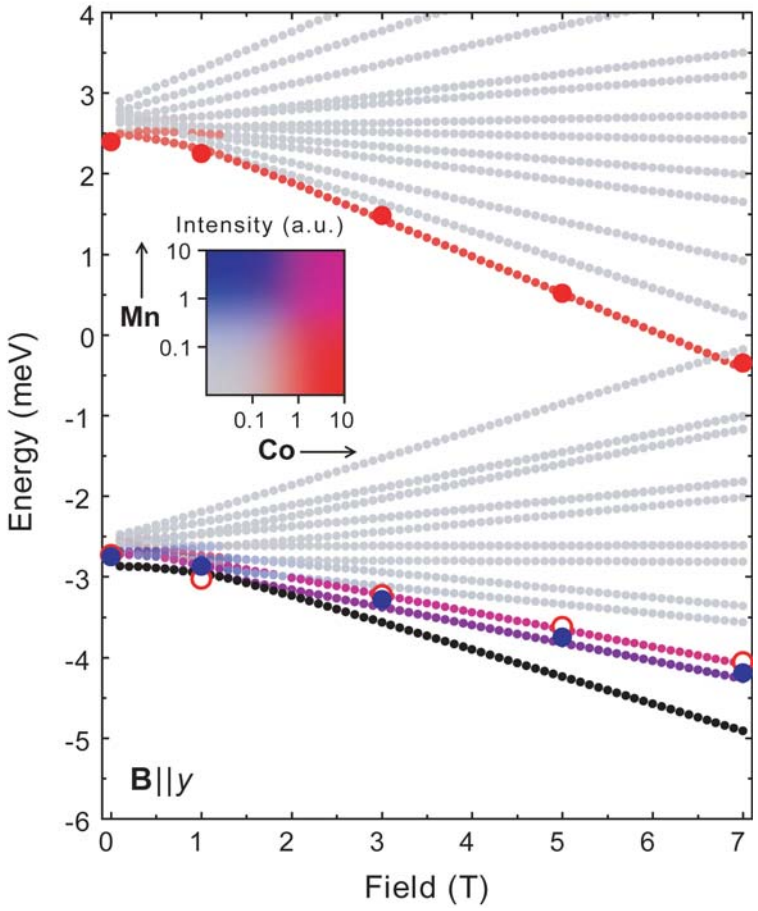

Figure 4.13: Eigenvalues of (4.22) with $J = 0.03$ meV, $g_{\mathrm{Mn}} = 1.90$, $g_{\mathrm{Co}} = 2.16$, $D_{\mathrm{Mn}} = -0.04$ meV and $D_{\mathrm{Co}} = 2.65$ meV for $\mathbf{B} \parallel y$. Experimental data points extracted from figs. 4.8c (blue) and d (red). **Inset:** key for the color representation of $I^{(\mathrm{Co})}_{0\to n}$ and $I^{(\mathrm{Mn})}_{0\to n}$.

thus represented by an effective field $\mathbf{B}_{\mathrm{eff}} = -J\mathbf{S}^{(\mathrm{X})}/g_{\mathrm{Co}}\mu_B$, corresponding to a magnitude of 2.1 T for Fe and 0.6 T for Mn.

The Heisenberg Kondo Dimer

The notion of coupling multiple Kondo systems has been considered by many theorists in a model that is known as the *Kondo Lattice* [83]. Especially interesting is the case where the coupling strength between spins can be tuned [84], which was realized experimentally in a quantum dot dimer [62]. Although tunable coupling is not readily available in our $\mathrm{Co_{vv}Co}$ structures, their properties

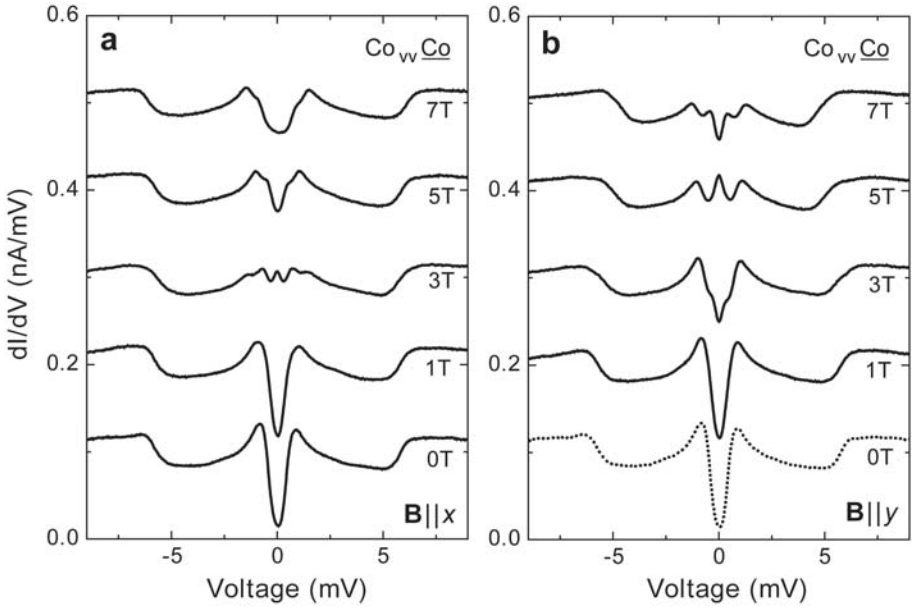

Figure 4.14: dI/dV-spectra measured on one of the Co atoms in $Co_{vv}Co$ at various magnetic fields oriented along x **(a)** and y **(b)**. The dotted spectrum in (b) was taken on a different structure than the others in the same panel. Since the field direction is irrelevant at zero field, this particular curve was measured over the atom neighboring the one in panel (a).

might provide valuable insights in the context of Kondo Lattices. Figure 4.14 shows field-dependent measurements performed on one of the two Co atoms in either $Co_{vv}Co$ dimer of fig. 4.6b, i.e. for $\mathbf{B} \parallel x$ and y. The spectra taken at 0 T are characterized by a remarkably deep dip at zero bias that is somewhat reminiscent of a band gap. At higher field strengths multiple small peaks seem to cross each other at various energies. We will attempt to model this with yet another variation of the full Heisenberg Hamiltonian:

$$\begin{aligned} \hat{\mathcal{H}} &= J\hat{\mathbf{S}}^{(\mathrm{Co1})} \cdot \hat{\mathbf{S}}^{(\mathrm{Co2})} - g_{\mathrm{Co}}\mu_B \mathbf{B} \cdot \left(\hat{\mathbf{S}}^{(\mathrm{Co1})} + \hat{\mathbf{S}}^{(\mathrm{Co2})}\right) \\ &\quad + D_{\mathrm{Co}} \left(\hat{S}_y^{2(\mathrm{Co1})} + \hat{S}_y^{2(\mathrm{Co2})}\right), \end{aligned} \tag{4.24}$$

where the superscript (Co1) or (Co2) indicates which of the two Co spins an operator works on. Surprisingly, as shown in figs. 4.15 and 4.16, this simple two-spin Hamiltonian can once again assign each observed spin excitation or resonance to an allowed transition within its eigensystem. Here the lower four states are all linear combinations of $|m_{\mathrm{Co1}}\ m_{\mathrm{Co2}}\rangle = |\pm\frac{1}{2} \pm \frac{1}{2}\rangle$ (where m_{Co1} and m_{Co2} refer to the eigenvalues of $\hat{S}_y^{(\mathrm{Co1})}$ and $\hat{S}_y^{(\mathrm{Co2})}$ respectively), whereas during the higher-energy excitations one of the two Co spins is rotated towards its hard-axis. In this situation a best fit is found for $J = 0.25 \pm 0.04$ meV.

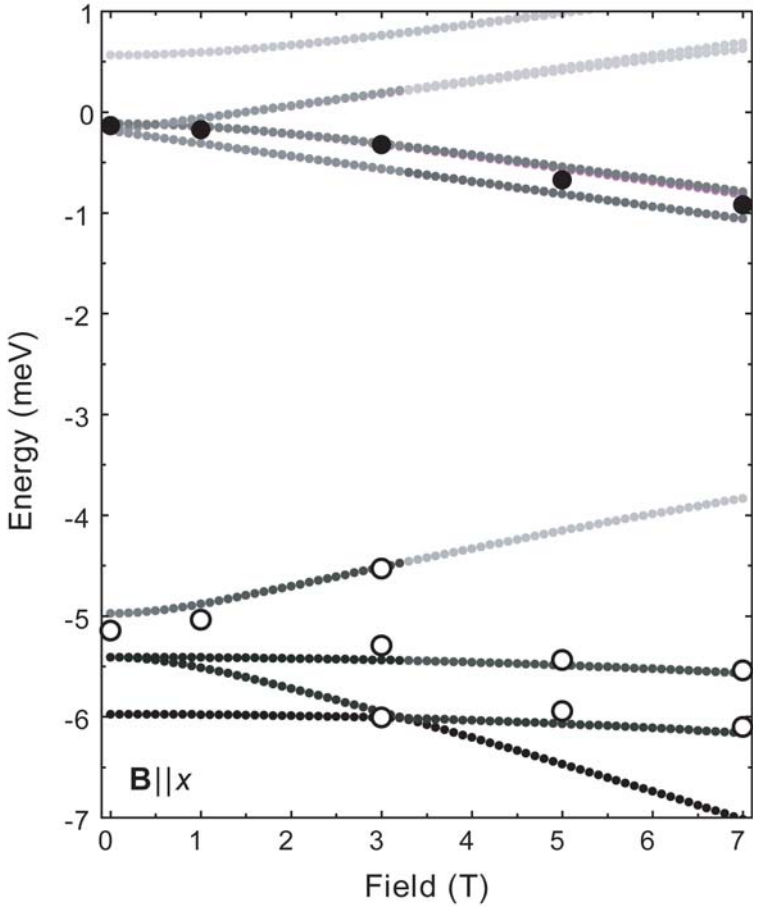

Figure 4.15: Lowest 12 eigenvalues of (4.24) with $J = 0.25$ meV, $g_{\mathrm{Co}} = 2.16$ and $D_{\mathrm{Co}} = 2.70$ meV for $\mathbf{B} \parallel x$. For each level $|\psi_n\rangle$ the corresponding transition intensity $I^{(\mathrm{Co})}_{0\to n}$ is shown in greyscale (see fig. 4.16 for key). Experimental data points extracted from fig. 4.14a plotted with respect to the calculated ground state where open (*filled*) circles represent peak (*step*) positions.

A remarkable exception to the overall good agreement between the measurements and the model occurs among the high-energy excitations for $B < 4.5$ T along y (fig. 4.16). According to the intensity calculations an additional excitation should take place between 6.0 and 6.5 meV. It is unclear why this is not observed through spectroscopy.

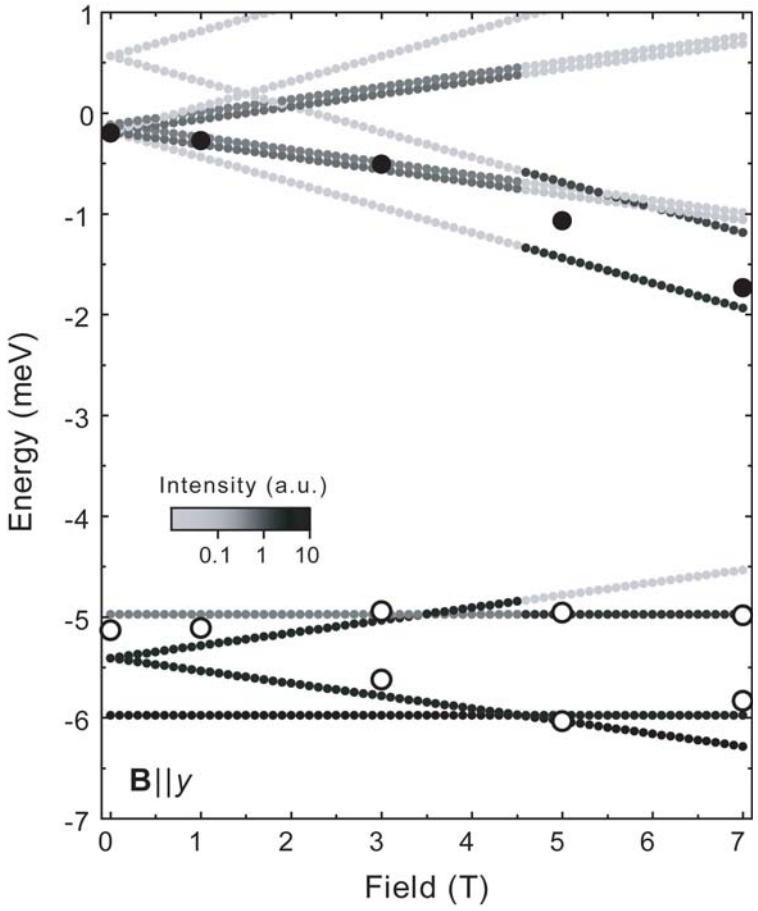

Figure 4.16: Lowest 12 eigenvalues of (4.24) with $J = 0.25$ meV, $g_{\mathrm{Co}} = 2.16$ and $D_{\mathrm{Co}} = 2.70$ meV for $\mathbf{B} \parallel y$. Experimental data points extracted from fig. 4.14b. **Inset:** key for the greyscale representation of $I^{(\mathrm{Co})}_{0\to n}$.

4.4 Discussion

The Kondo effect results from a resonant interaction between a spin and its surrounding conduction electrons. It is a complex many-body phenomenon that even after decades of research remains topic of debate. The work presented in this chapter might be a valuable contribution to this discussion. We have studied a single magnetic atom with a known high spin in an anisotropic environment that was thoroughly analyzed beforehand. We understand exactly how the crystal field anisotropy effectively reduces the spin to an $S = \frac{1}{2}$ Kramers doublet thus creating a Kondo system, and why other magnetic atoms in the same situation do not show such behavior. If a magnetic field is applied the Kondo resonance

splits in a manner that precisely reflects the magnetically anisotropic nature of the system consisting of the spin and its environment. And finally, if a second magnetic atom is positioned in the vicinity of the Kondo spin the resulting changes in the energies at which the resonances take place can be fully modelled by isotropic Heisenberg coupling of two anisotropic spins. Surprisingly, this is true even if the second spin is a Kondo spin itself.

The various $X_{vv}Co$ structures form a unique class of nano-objects. The energy scales involved in the coupling process (i.e. J) are of the same magnitude as all the other relevant processes in the system (D, E, $\mu_B B$), yet the spins are coupled weakly enough and are sufficiently far apart such that each can be addressed separately by the STM tip. As we have concluded from DFT studies in the previous chapter, the adatoms are incorporated into a large molecular network. Hence the dimers discussed here can be regarded as molecular magnets where each of the magnetic centers can be studied on its own.

While we can successfully model the interaction with an empirical Heisenberg constant J, the physics of the coupling remains unclear. According to classical electrodynamics the dipole $\boldsymbol{\mu} = -e\mathbf{S}/m_e$ formed by an electron spin $\mathbf{S}$ (where m_e is the electron mass) sets up a magnetic field

$$\mathbf{B} = \frac{\mu_0}{4\pi r^3}\Big(3(\boldsymbol{\mu}\cdot\hat{r})\hat{r} - \boldsymbol{\mu}\Big) \tag{4.25}$$

at a position $\mathbf{r}$ relative to the spin (if $r > 0$). Here μ_0 is the permeability of vacuum and $\hat{r} = \mathbf{r}/r$. In case of $S = 2$ and $r = 7.2$ Å the magnitude of such a field cannot exceed 4×10^{-2} T which is 50 times lower than the 2.1 T we encounter. This rules out dipolar interaction as the dominant mediator for our J, which means that the spins have to be coupled somehow by exchange interaction through the Cu_2N surface. In the following chapter we will discuss some initial investigations into the mechanism of spin coupling on Cu_2N.